Magnetic and electric field dependent anisotropic magnetoelectric multiferroicity in $SmMn_3Cr_4O_{12}$

Guangxiu Liu,[1,2] Zhehong Liu,[1,2] Yisheng Chai,[3,4] Long Zhou,[1] Xudong Shen,[1,5] Xubin Ye,[1,2] Shijun Qin,[1,2] Dabiao Lu,[1,2] Zhiwei Hu,[6] Liu Hao Tjeng,[6] Hong-Ji Lin,[7] Chien-Te Chen,[7] Xiaohui Yu,[1,2] and Youwen Long[1,2,5,*]

[1]*Beijing National Laboratory for Condensed Matter Physics, Institute of Physics, Chinese Academy of Sciences, Beijing 100190, China*
[2]*School of Physical Sciences, University of Chinese Academy of Sciences, Beijing 100049, China*
[3]*Center of Quantum Materials and Devices, Chongqing University, Chongqing 401331, China*
[4]*Low Temperature Physics Laboratory and Chongqing Key Laboratory of Soft Condensed Matter Physics and Smart Materials, College of Physics, Chongqing University, Chongqing 401331, China*
[5]*Songshan Lake Materials Laboratory, Dongguan, Guangdong 523808, China*
[6]*Max Planck Institute for Chemical Physics of Solids, Dresden 01187, Germany*
[7]*National Synchrotron Radiation Research Center, Hsinchu 30076, Taiwan*

(Received 17 May 2021; accepted 19 July 2021; published 5 August 2021)

An *A*-site ordered perovskite $SmMn_3Cr_4O_{12}$ with a cubic *Im*-3 space group was prepared at high pressure and temperature conditions. Two antiferromagnetic phase transitions are found to occur with decreasing temperature to $T_{N1} \approx 145$ K and $T_{N2} \approx 41$ K, due to the spin orderings of the *B*-site Cr^{3+} and *A*′-site Mn^{3+} magnetic sublattices, respectively. The total spin structure composed of these two magnetic sublattices can break the space inversion symmetry and therefore induce a spontaneous ferroelectric phase transition at T_{N2}. More interestingly, the magnetoelectric multiferroicity of the polycrystalline $SmMn_3Cr_4O_{12}$ exhibits remarkable magnetic and electric field dependent anisotropic quadratic behaviors upon a proper magnetoelectric poling procedure. When the applied magnetic field is parallel to the electric field, the magnetic field can significantly enhance the electric polarization. In contrast, the polarization is sharply suppressed if the magnetic field is perpendicular to the electric field, irrespective of the sign of the magnetic field.

DOI: 10.1103/PhysRevB.104.054407

I. INTRODUCTION

Magnetoelectric (ME) multiferroics simultaneously possess long-range ferroelectric and magnetic orders where electric polarization can be switched by a magnetic field, and magnetization can be switched by an electric field reversely [1–16]. As a result, multiferroic materials are promising for potential applications in developing multiple-state memory devices, magnetic sensors, resonators, spintronic devices, and so on [17–20]. In particular, if a spin structure breaks the space inversion symmetry and induces a spontaneous ferroelectric polarization, strong ME coupling can be achieved. Taking $TbMnO_3$ [21,22] as an example, the Mn^{3+} spins show a sinusoidal antiferromagnetic (AFM) ordering with a wave vector $(0, k_s, 1)$ at the onset temperature of 41 K. Once the modulation wave vector k_s locks to be about 0.28 at 27 K, the magnetic structure is transformed into a spiral AFM ordering, which gives rise to a sharp ferroelectric phase transition with a strong ME effect. Despite the interesting physical properties as well as the potential applications, the amount of spin-induced single-phase multiferroic materials is limited due to the complex spin structures as required by the related multiferroic mechanisms such as spin-current model or inverse Dzyaloshinskii-Moriya interaction [23–25], exchange striction mechanism [26,27], and spin-dependent *p-d* hybridization model [28,29].

Although the above three microscopic origins can describe most of spin-induced ferroelectricity for multiferroics, an exception was discovered in $LaMn_3Cr_4O_{12}$ (LMCO) [30] with cubic *A*-site ordered quadruple perovskite structure $AA'_3B_4O_{12}$ [31–34]. A new mechanism, i.e., anisotropic symmetric exchange [35], was proposed by Feng and Xiang to explain the spin-driven ferroelectricity of LMCO. In LMCO, the *A*′-site Mn^{3+} and *B*-site Cr^{3+} spins separately form a nonpolar collinear *G*-type AFM ordering, but the combination of them shows a polar magnetic point group which can generate a spontaneous ferroelectric polarization. Thus, a considerable ME coupling is observed in this compound although the value of polarization is relatively small. Considering the highly symmetric cubic structure of LMCO, the polarization is ascribed to a pure electronic contribution. When *A*-site La^{3+} ion is replaced by Bi^{3+} ion with $6s^2$ lone-pair electrons, the electric polarization induced by collinear AFM spins as that of LMCO, and Bi^{3+}-induced ferroelectricity like $BiFeO_3$ [36,37] and $BiMnO_3$ [38–40], simultaneously exist in $BiMn_3Cr_4O_{12}$ (BMCO) [41]. Consequently, both strong ME effect and large polarization are achieved in the single-phase material of BMCO. The result means that the *A*-site atom plays an important role in the ME properties in the $AMn_3Cr_4O_{12}$ family.

Since both La^{3+} and Bi^{3+} are nonmagnetic, the possible effect of *A*-site magnetism on the polar spin structure remains to be evaluated in the $AMn_3Cr_4O_{12}$ family. Taking into account that Sm^{3+} ion has a relatively small effective magnetic moment ($0.85\,\mu_B$) among rare earths with +3 valence state, this magnetic ion was adopted to occupy the *A* site,

*Corresponding author: ywlong@iphy.ac.cn

 ©2021 American Physical Society

and $SmMn_3Cr_4O_{12}$ (SMCO) was prepared under high pressure and temperature conditions in this work. SMCO displays similar crystal structure as well as magnetic phase transitions and spin-induced ferroelectric polarization as those observed in LMCO. Unexpectedly, however, after a proper ME poling process, strongly anisotropic quadratic ME effects are found to occur in SMCO, as featured by sharply enhanced or suppressed electric polarization with different magnetic and electric field configurations regardless of the isotropic nature of the polycrystalline specimen.

II. EXPERIMENTAL METHODS

We prepared polycrystalline SMCO, using starting materials of highly pure Sm_2O_3, Mn_2O_3, Cr_2O_3 powders in a 1:3:4 mole radio, at high-temperature and -pressure conditions. These reactants were thoroughly ground and then sealed into a gold capsule with 3.0 mm in diameter and 4.0 mm in length. The capsule was heated to 1373 K at 7 GPa for 30 min on a cubic anvil-type high-pressure apparatus. The crystal structure was checked by powder x-ray diffraction (XRD) using a Huber diffractometer equipped with Cu $K\alpha_1$ radiation at 40 kV and 30 mA at room temperature. The GSAS program was applied to refine the structural parameters based on the Rietveld method [42]. Soft x-ray absorption spectroscopy (XAS) at the Cr-$L_{2,3}$ and Mn-$L_{2,3}$ edges was measured at beamline TLS11A of the National Synchrotron Radiation Research Center in Taiwan.

The temperature-dependent magnetic susceptibility at zero-field-cooling (ZFC) mode and field-dependent magnetization were measured on a magnetic property measurement system (MPMS-VSM, Quantum Design). The specific heat was measured on a physical property measurement system (PPMS-9T, Quantum Design) using a pulse relaxation method. A specimen of 0.25-mm-thickness disk shape was prepared to measure electrical properties. This disk was polished to mirror and then silver paste electrodes were painted on the bottom and top surfaces of the disk. The relative dielectric constant was measured at different frequencies and magnetic fields via an Agilent-4980A LCR meter. After poling the sample under a selected magnetic field and an electric field $E = 8\,\mathrm{kV/cm}$ from 50 to 2 K, and waiting for half an hour in electrical short circuit to exclude possible extrinsic contributions, the pyroelectric current was measured using a Keithley 6517B electrometer on warming the sample. During the measurement, the applied magnetic field was not removed until the pyroelectric current measurement was finished up to 50 K. The electrical polarization was calculated by integrating the measured current data. The isothermal polarized current between 9 and −9 T was measured after being electrically poled to 5 K under zero magnetic field; then, polarization was obtained by integrating the polarized current as a function of time.

III. RESULTS AND DISCUSSION

Figure 1(a) shows the XRD pattern and the refinement result of SMCO at room temperature. All the peaks can be well indexed based on a cubic symmetry. The Rietveld analysis demonstrates that the compound crystallizes in an

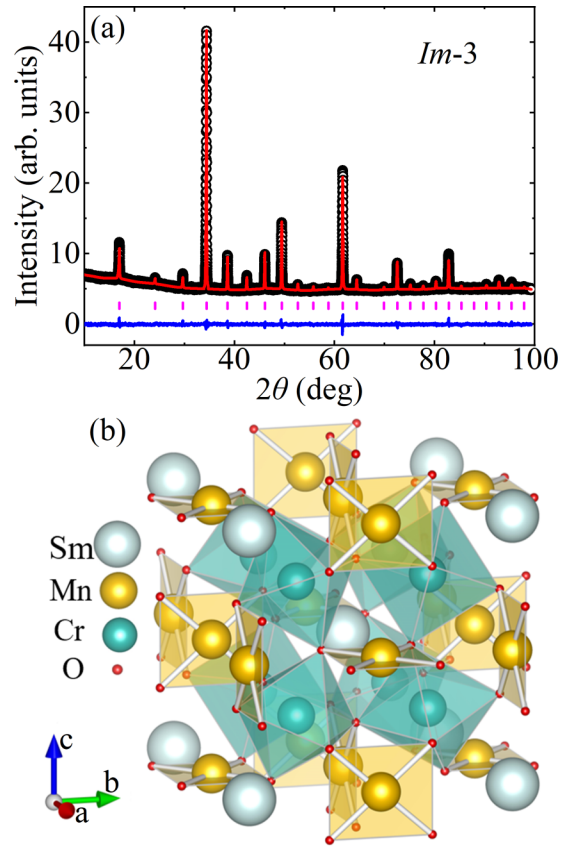

FIG. 1. (a) Rietveld refinement of the powder XRD data of SMCO measured at room temperature. The observed (black circle), calculated (red line), difference (blue line), and allowed Bragg reflections (ticks) by space group *Im*-3 are presented. (b) Schematic crystal structure of SMCO. CrO_6 octahedra connected by a corner-shared network and MnO_4 square planes are shown.

A-site ordered perovskite structure with a chemical formula of $AA'_3B_4O_{12}$ [see Fig. 1(b)]. The space group is a cubic *Im*-3 with central symmetry, where Sm and Mn are 1:3 ordered at specific Wyckoff sites 2*a* (0, 0, 0) and 6*b* (0, 0.5, 0.5), and Cr and O at special 8*c* (0.25, 0.25, 0.25) and 24*g* (*x*, *y*, 0) sites, respectively. Compared with a simple ABO_3 perovskite, the introduction of a transition metal into the A' site in the ordered $AA'_3B_4O_{12}$ perovskite causes the formation of square-coordinated $A'O_4$ units and heavily tilted BO_6 octahedra, as described in detail elsewhere [31–34]. The refined structural parameters of SMCO are listed in Table I. A satisfying fitting goodness parameter of R_{wp} is obtained by 1.66%. The lattice constant of SMCO is 7.366 03(1) Å, which is slightly less than that of LMCO ($a = 7.398\,32$ Å) [43] due to the reduced ionic size of Sm with regard to La. According to the refined Cr–O and Mn–O bond lengths, the bond valence sum (BVS) calculations illustrate that the valence states of Mn and Cr are both close to +3 (see Table I), as revealed by soft x-ray XAS results shown below.

The XAS of 3*d* transition metal at the $L_{2,3}$ edges is sensitive to its valence state [44–46] and local environment [47,48]. In general, when the valence state increases, the absorption peak remarkably shifts towards higher energies. Figure 2(a) shows the Cr-$L_{2,3}$ absorption spectrum of SMCO,

TABLE I. Refined structural parameters for SMCO at room temperature. Atomic sites: Sm 2*a* (0, 0, 0), Mn 6*b* (0, 0.5, 0.5), Cr 8*c* (0.25, 0.25, 0.25), and O 24*g* (*x*, *y*, 0). BVS values (V_i) were calculated via formula $V_i = \sum_j S_{ij}$ and $S_{ij} = \exp[(r_0 - r_{ij})/0.37]$ using parameters $r_0(Mn^{3+}) = 1.732$ Å and $r_0(Cr^{3+}) = 1.708$ Å.

Parameters	$SmMn_3Cr_4O_{12}$
a (Å)	7.366 03(1)
V (Å^3)	399.669(2)
O_x	0.304 9(2)
O_y	0.169 8(2)
U_{iso}(Sm)(100×Å^2)	2.35(2)
U_{iso}(Mn)(100×Å^2)	2.64(3)
U_{iso}(Cr)(100×Å^2)	2.51(3)
U_{iso}(O)(100×Å^2)	2.48(7)
Mn-O(×4) (Å)	1.905(1)
(×4) (Å)	2.825(2)
(×4) (Å)	3.311(2)
Cr-O(×6) (Å)	1.975(1)
∠Cr-O-Cr(°)	137.5(1)
BVS (Mn)	2.77
BVS (Cr)	2.91
R_{wp} (%)	1.66
R_p (%)	1.2

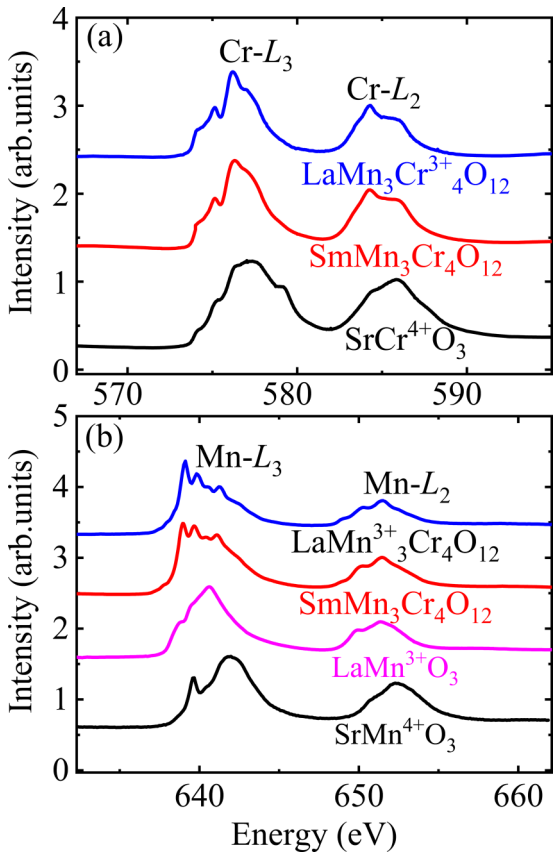

FIG. 2. XAS spectra of (a) Cr-$L_{2,3}$ and (b) Mn-$L_{2,3}$ edges measured at room temperature for SMCO. For comparison, XAS spectra of $LaMn_3Cr_4O_{12}$, $SrCrO_3$, $LaMnO_3$, and $SrMnO_3$ are used as references.

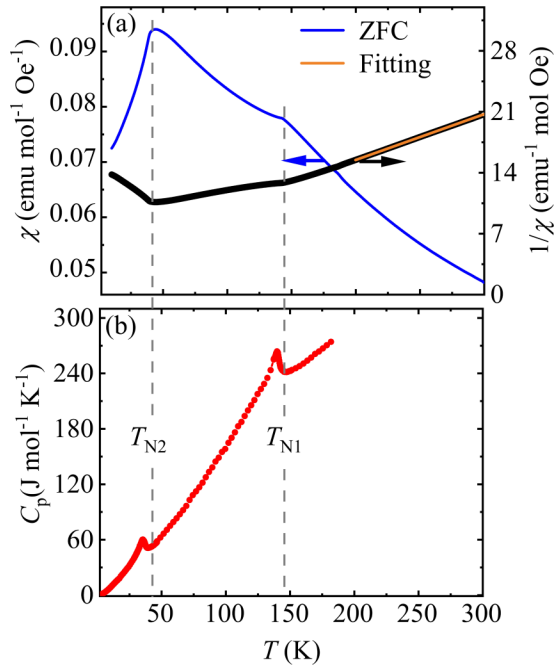

FIG. 3. (a) Temperature dependence of magnetic susceptibility χ measured at 0.1 T for SMCO. The yellow line shows the Curie-Weiss fitting of $1/\chi$ above 200 K. (b) Temperature-dependent specific heat C_p of SMCO measured from 2 to 180 K at zero magnetic field.

using LMCO as a Cr^{3+} reference [43] and $SrCrO_3$ as a Cr^{4+} reference with similar CrO_6 octahedral coordination. Compared with the Cr^{4+} reference, the spectrum of SMCO apparently shifts towards lower energies, indicating a relatively low Cr valence [49,50]. However, the multiple spectral features and the energy position of SMCO are the same as those of the Cr^{3+} reference LMCO, meaning the formation of a Cr^{3+} valence state at the octahedral *B* site in SMCO. To identify the Mn valence state in SMCO, LMCO [43] as a Mn^{3+} reference with MnO_4 planar square, $LaMnO_3$ as a Mn^{3+} reference, and $SrMnO_3$ as a Mn^{4+} reference [51] with MnO_6 octahedral coordination environments are presented in Fig. 2(b) for comparison. Obviously, the spectrum of SMCO shifts to a lower energy relative to that of $SrMnO_3$, but locates at the same energy as $LaMnO_3$, suggesting the formation of Mn^{3+} valence state. It is noticeable that the multiple spectral feature of SMCO is very different from that of $LaMnO_3$, but the same as that of LMCO, indicating the presence of a Mn^{3+} at the square-coordinated *A′* site [see Fig. 2(b)]. The XAS measurements thus confirm the charge combination to be $SmMn^{3+}{}_3Cr^{3+}{}_4O_{12}$, which is identical with that observed in LMCO [43].

Figures 3(a) and 3(b) show the temperature dependence of magnetic susceptibility and specific heat of SMCO, respectively. With decreasing temperature to $T_{N1} \approx 145$ K, the magnetic susceptibility curve shows an apparent kink, indicating the formation of an AFM phase transition. The sharp λ-type anomaly observed in specific heat further confirms the long-range magnetic transition occurring at T_{N1}. On further cooling to $T_{N2} \approx 41$ K, both susceptibility and specific heat show a clear anomaly, illustrating a second long-range AFM

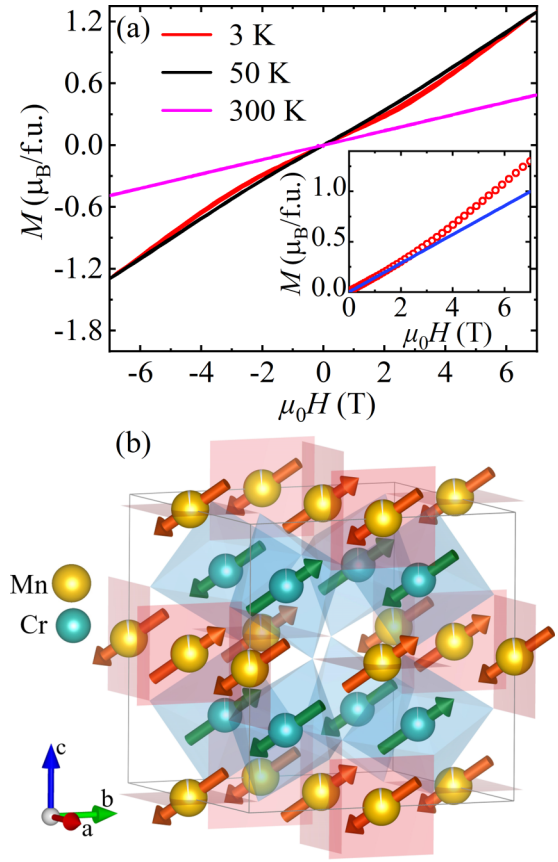

FIG. 4. (a) Field-dependent magnetization of SMCO measured at some selected temperatures. The inset shows the deviation of magnetization from the linear relationship near 2.5 T at 3 K, suggesting a field-induced metamagnetic transition. (b) Schematic illustration of total spin structure composed of Mn^{3+} and Cr^{3+} magnetic sublattices for SMCO.

phase transition. Below T_{N2}, the specific heat just smoothly decreases, ruling out the occurrence of Sm^{3+} spin ordering at lower temperatures. If the inverse susceptibility as a function of temperature is plotted [see Fig. 3(a)], one finds that the data above 200 K well follow the Curie-Weiss law with the function $\chi^{-1} = (T\text{-}\theta)/C$. The fitting gives a negative Weiss temperature $\theta = -94.4$ K, indicating the dominance of AFM interactions between magnetic moments. According to the fitted Curie constant ($C = 19.02$ emu K mol^{-1} Oe^{-1}), the effective magnetic moment is calculated to be $\mu_{\text{eff}} = 12.33\,\mu_B$/f.u. This value is comparable with the theoretical one ($11.52\,\mu_B$/f.u.) if we consider the contributions of the A-site Sm^{3+}, A'-site Mn^{3+}, and B-site Cr^{3+} magnetic ions.

Figure 4(a) shows the field-dependent magnetization curves measured at different temperatures. In accordance with the paramagnetism, linear magnetization behavior is observed above T_{N1}, e.g., at 300 K. Between T_{N1} and T_{N2} such as at 50 K, the magnetization also exhibits a linear relationship with field. A long-range AFM ordering is thus assigned to the magnetic transition occurring at $T_{N1} \sim 145$ K. Again, at 3 K, the magnetization linearly changes with field below ~2.5 T, in agreement with the second long-range AFM phase transition occurring at $T_{N2} \sim 41$ K. At higher fields, however, the magnetization at 3 K slightly deviates from the linear behavior [see the inset of Fig. 4(a)]. Such a metamagnetic transition may be attributed to a field-induced magnetization of Sm^{3+}, or possible spin flop of Mn^{3+} and/or Cr^{3+} ions. The magnetic and specific-heat measurement results demonstrate that SMCO experiences similar magnetic phase transitions with those observed in LMCO. Since the two compounds also have identical crystal structure with Im-3 symmetry, comparable spin structures would be expected to occur. By analogy with LMCO [30,43], the AFM transition at T_{N1} in SMCO should be ascribed to the collinear G-type spin ordering of B-site Cr^{3+} moments. The other AFM transition occurring at T_{N2} is caused by the A'-site Mn^{3+} spins in a G-type manner, too. Figure 4(b) represents the detailed spin structure of SMCO. A single Mn^{3+} or Cr^{3+} magnetic sublattice arranges in a G-type AFM manner with the spin moments along the crystal [111] direction. Although each sublattice itself has a nonpolar magnetic structure, the total collinear spin structure composed of Mn^{3+} and Cr^{3+} sublattices can form a type-II polar magnetic point group **31′** and break the space inversion symmetry. As a result, a spin-induced ferroelectric polarization is expected to occur below T_{N2}.

To confirm the spin-induced polarization, temperature and field-dependent relative dielectric constant and pyroelectric current were measured for SMCO. Figure 5(a) shows the temperature dependence of relative dielectric constant measured at different frequencies and zero field. Corresponding to the AFM phase transition, a sharp dielectric peak is found to occur at $T_{N2} \approx 41$ K (no dielectric anomaly occurring at T_{N1}, not shown here). Moreover, the dielectric peak is frequency independent. When a magnetic field $\mu_0 H$ and an electric field E are simultaneously applied to measure the dielectric constant, one can find apparent anisotropic behavior. Specifically, the dielectric peak becomes sharper with $\mu_0 H$ up to 6 T if $\mu_0 H \| E$ [see Fig. 5(b)]. In contrast, however, the $\mu_0 H$ significantly suppresses the dielectric peak in a $\mu_0 H \perp E$ configuration, where only a small anomaly emerges with $\mu_0 H$ up to 6 T [see Fig. 5(c)]. The dielectric measurement results strongly suggest the occurrence of a spin-induced ferroelectric polarization as well as anisotropic ME properties of SMCO in its polycrystalline form.

To get deeper insight into the magnetic and electric field dependent polarization, the pyroelectric current I_p was measured using $\mu_0 H \| E$ and $\mu_0 H \perp E$ configurations at several fixed magnetic fields. Figure 6(a) shows the temperature-dependent I_p with $\mu_0 H \| E$. The I_p is exactly zero at higher temperatures ($>T_{N2}$). However, it sharply increases at the onset of T_{N2} and forms a peak slightly less than this AFM ordering temperature. Moreover, in this $\mu_0 H$ and E configuration, applying a $\mu_0 H$ significantly enhances the I_p. By integrating the I_p as a function of time, we obtain the electric polarization P as presented in Fig. 6(b). Obviously, both the I_p and P are completely reversible without changing the magnitudes if the sign of the poling electric field is reversed. Therefore, a spin-induced ferroelectric phase transition is confirmed to take place at T_{N2}. With increasing $\mu_0 H$ from 0 to 6 T, the P increases from 77 to 130 μC/m^2. On the other hand, if the applied $\mu_0 H$ is perpendicular to E during the I_p measurement, one finds that the magnetic field drastically suppresses the I_p. As shown in Fig. 7(a), the sharp I_p peak near T_{N2} is reduced to a smaller one when a 6-T magnetic field

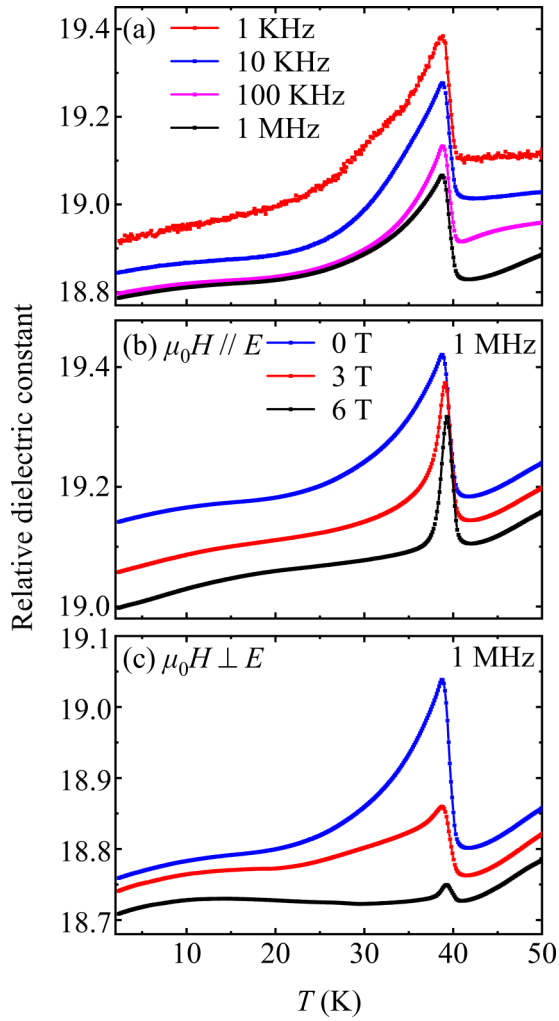

FIG. 5. (a) Temperature-dependent relative dielectric constant ε_r of SMCO measured at different frequencies and 0 T. The same parameter measured at different magnetic fields and 1 MHz with (b) magnetic field parallel to electric field (8 kV/m), and (c) perpendicular to the electric field. The data are shifted for clarity.

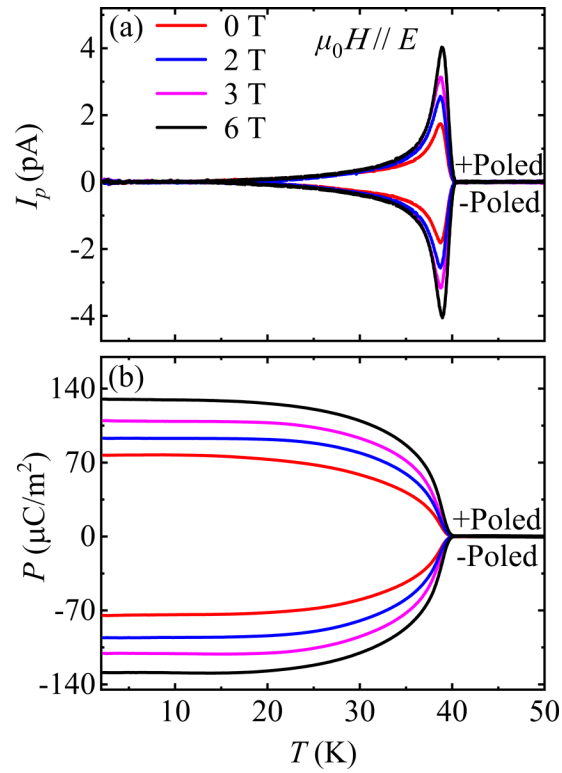

FIG. 6. Temperature-dependent (a) pyroelectric current I_p, and (b) ferroelectric polarization P in both +poled and −poled conditions measured at various magnetic fields. The poling electric field $E = 8\,\mathrm{kV/cm}$ is applied in parallel to $\mu_0 H$ with temperature cooling from 50 to 2 K, and the polarization P is obtained by integrating the current as a function of time.

is applied. Correspondingly, the magnitude of P decreases from 77 μC/m^2 at $\mu_0 H = 0$ to 28.5 μC/m^2 at $\mu_0 H = 6$ T [see Fig. 7(b)], indicating that the magnetic field can significantly suppress the electric polarization in the $\mu_0 H \perp E$ configuration, in agreement with the observation in dielectric constant measurements. Note that when $\mu_0 H$ and E have a tilted angle of 45 °, the related electric polarization is located at the intermediate between those observed in $\mu_0 H$ parallel and perpendicular to E configurations (not shown here).

We now discuss possible origins for the anisotropic magnetoelectric behavior of SMCO. Given the same crystal and spin structures for SMCO and LMCO, the ferroelectric polarization of SMCO can also be attributed to the collinear spin arrangement composed of the Mn^{3+} and Cr^{3+} spin sublattices together. This means that the proposed mechanism for ferroelectricity in LMCO [35] is also valid for SMCO. The proposed spin structure of SMCO has a type-II magnetic point group of **31′**, in which a threefold rotation axis forms along the crystal [111] direction with an independent time-reversal symmetry. For the type-II magnetic point group, no linear ME tensor is allowed. The matrix form of quadratic ME tensors for the magnetic point group **31′** is

$$B = \begin{bmatrix} \beta_{11} & -\beta_{11} & 0 & \beta_{14} & \beta_{15} & -2\beta_{22} \\ -\beta_{22} & \beta_{22} & 0 & \beta_{15} & -\beta_{14} & -2\beta_{11} \\ \beta_{31} & \beta_{31} & \beta_{33} & 0 & 0 & 0 \end{bmatrix}. \quad (1)$$

According to the Neumann principle, the ME tensor is invariant under every permissible symmetry operation of the given magnetic point group for a crystal, which significantly restricts the independence of these coefficients in a ME tensor and then the tensor can only be nonzero in some magnetic point groups [52,53]. The above ME tensor for the polar point group **31′** allows the presence of electric polarization and quadratic magnetoelectric effect. Moreover, the quadratic ME coupling coefficient $\beta = d^2P/dH^2$ is a third-rank polar tensor [6,54].

To further identify the quadratic ME effect of SMCO, by scanning the magnetic field at a fixed temperature of 5 K, the electric polarization was also measured at $\mu_0 H \| E$ and $\mu_0 H \perp E$ configurations. This measurement was performed using the same specimen that was measured at fixed magnetic fields mentioned above. As shown in Fig. 8, the $\mu_0 H$ applied along the direction of the poling electric field (i.e., $\mu_0 H \| E$) can enhance the polarization P considerably, irrespective of the sign of H, and the P is almost saturated

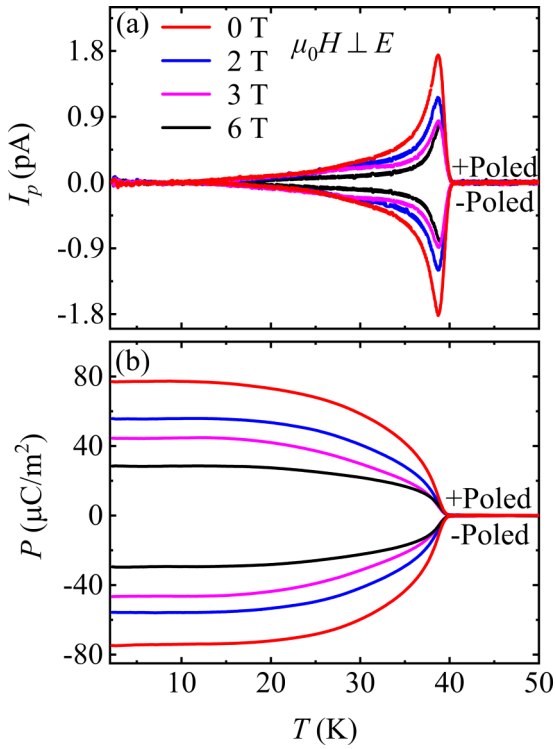

FIG. 7. Temperature-dependent (a) pyroelectric current I_p, and (b) ferroelectric polarization P of +poled and −poled conditions collected at different magnetic fields. The poling electric field $E = 8\,\mathrm{kV/cm}$ is applied perpendicular to $\mu_0 H$.

to be about $105\,\mu\mathrm{C/m^2}$ as the $\mu_0 H$ increases to 6 T. In sharp contrast, the polarization is remarkably reduced when the $\mu_0 H$ applied is perpendicular to the direction of E (i.e., $\mu_0 H \perp E$), so that the P almost decreases to $48\,\mu\mathrm{C/m^2}$ with the magnitude of the field up to 6 T. These observations provide convincing evidence for the magnetic and electric field dependent anisotropic ME multiferroicity of SMCO. Furthermore, between −2.5 and 2.5 T, the variation of polarization $\Delta P[= P(\mu_0 H)\text{-}P(0\,\mathrm{T})]$ in $\mu_0 H \| E$ mode upon scanning the magnetic field can be well fitted by the function

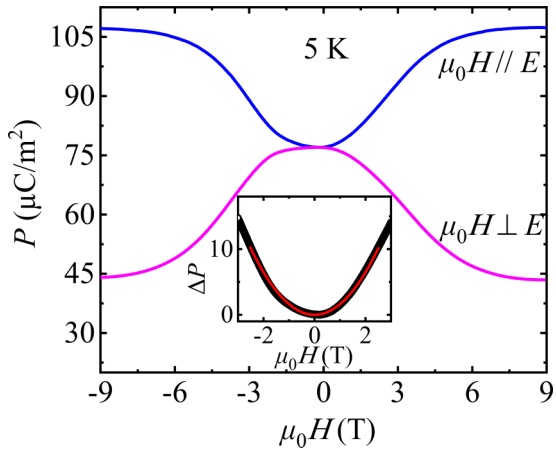

FIG. 8. Magnetic field dependent polarization P at 5 K measured in $\mu_0 H \| E$ and $\mu_0 H \perp E$ configurations. The value of applied E is 8 kV/cm. The inset shows the fitting result (red line) for the data of ΔP (black circle) using the function $\Delta P = \beta H^2$ as described in text.

of $\Delta P = \beta H^2$ [55,56] with the second-order ME coefficient $\beta = 2.56\times10^{-18}$ s/A [see the inset of Fig. 8]. The fitting result shows that the quadratic ME effect governs the ME property of SMCO, whereas the linear one is negligible within ±2.5 T. It also agrees well with the fact that the magnetic point group **31′** of SMCO allows only the even-order ME effects. At higher fields, however, the field-dependent polarization gradually deviates from the quadratic behavior and the magnitude of polarization becomes saturated around 6 T. If one compares the field-dependent polarization (see Fig. 8) and magnetization [see Fig. 4(a)], it seems that the deviation from quadratic ME effect at higher magnetic field may be related to the field-induced metamagnetism around 2.5 T. Note that the evolution of P is similar under positive and negative H in both $\mu_0 H \perp E$ and $\mu_0 H \| E$ configurations in SMCO. The detailed mechanisms for the exceptional ME behaviors are deserved to be further investigated in the future, especially by theoretical analysis.

In addition, we have to emphasize the role of ME poling procedure for the observed anisotropic quadratic ME effects in SMCO. In principle, a polycrystalline SMCO with randomly oriented grains is not expected to show any ME effect due to the high symmetry caused by isotropic grain distribution. However, a proper ME poling procedure, by applying simultaneous electric and magnetic fields, will induce the nonzero ME tensors and detectable ME effect even in a polycrystalline sample if the ME tensor itself is nonzero in theory. In fact, the linear ME effect of polycrystalline Cr_2O_3 after ME poling has been observed experimentally and explained theoretically [57]. The same arguments on the role of ME poling can be applied to the quadratic ME effect of SMCO. Note that no theoretical expression for quadratic ME tensors is derived in isotropic polycrystalline materials as yet. The current SMCO provides a prototype cubic material system with remarkable magnetic and electric field dependent anisotropic magnetoelectric multiferroicity in its polycrystalline form.

IV. CONCLUSIONS

In conclusion, an *A*-site ordered perovskite $SmMn_3Cr_4O_{12}$ with a cubic *Im*-3 space group was prepared at high-pressure and temperature conditions. Both the BVS and XAS results demonstrate that the charge combination is $SmMn^{3+}{}_3Cr^{3+}{}_4O_{12}$. Magnetic susceptibility and specific heat illustrate that the compound experiences two long-range AFM phase transitions at $T_{N1} \approx 145\,\mathrm{K}$ and $T_{N2} \approx 41\,\mathrm{K}$, respectively. In analogy with the isostructural $LaMn_3Cr_4O_{12}$, the *B*-site Cr^{3+} and *A′*-site Mn^{3+} magnetic sublattices are responsible for these two spin orderings. Since the total spin structure of SMCO can break the space inversion symmetry, a spontaneous ferroelectric polarization is found to occur at T_{N2}. Moreover, by using a proper ME poling procedure, strongly magnetic and electric field dependent anisotropic ME properties are observed in the polycrystalline SMCO. In a $\mu_0 H \| E$ configuration, the spin-induced electric polarization can be significantly enhanced by a magnetic field. In sharp contrast, the polarization is suppressed by a magnetic field in a $\mu_0 H \perp E$ configuration. More interestingly, the exceptional quadratic anisotropic ME behavior shows up in SMCO, which essentially differs from most ME multiferroic materials.

ACKNOWLEDGMENTS

This work was supported by the Beijing Natural Science Foundation (Grant No. Z200007), the National Natural Science Foundation of China (Grants No. 11934017, No. 51772324, No. 11921004, No. 11574378, and No. 11974065), the National Key R&D Program of China (Grants No. 2018YFE0103200 and No. 2018YFA0305700), and the Chinese Academy of Sciences (Grants No. XDB33000000 and No. QYZDB–SSW–SLH013). We acknowledge support from the Max Planck-POSTECH-Hsinchu Center for Complex Phase Materials.

[1] I. E. Dzyaloshinskii, Sov. Phys. JETP **10**, 628 (1960).
[2] D. N. Astrov, Sov. Phys. JETP **11**, 708 (1960).
[3] H. Schmid, Ferroelectrics **162**, 317 (1994).
[4] M. Fiebig, J. Phys. D: Appl. Phys. **38**, R123 (2005).
[5] O. F. de Alcantara Bonfim and G. A. Gehring, Adv. Phys. **29**, 731 (2006).
[6] W. Eerenstein, N. D. Mathur, and J. F. Scott, Nature (London) **442**, 759 (2006).
[7] T. Kimura, Annu. Rev. Mater. Res. **37**, 387 (2007).
[8] S. W. Cheong and M. Mostovoy, Nat. Mater. **6**, 13 (2007).
[9] Y. Tokura, J. Magn. Magn. Mater. **310**, 1145 (2007).
[10] G. Srinivasan, Annu. Rev. Mater. Res. **40**, 153 (2010).
[11] Y. Tokura and S. Seki, Adv. Mater. **22**, 1554 (2010).
[12] Y. Tokura, S. Seki, and N. Nagaosa, Rep. Prog. Phys. **77**, 076501 (2014).
[13] S. Dong, J.-M. Liu, S.-W. Cheong, and Z. Ren, Adv. Phys. **64**, 519 (2015).
[14] M. Fiebig, T. Lottermoser, D. Meier, and M. Trassin, Nat. Rev. Mater. **1**, 16046 (2016).
[15] N. A. Spaldin and R. Ramesh, Nat. Mater. **18**, 203 (2019).
[16] S. Dong, H. Xiang, and E. Dagotto, Natl. Sci. Rev. **6**, 629 (2019).
[17] H. Béa, M. Gajek, M. Bibes, and A. Barthélémy, J. Phys.: Condens. Matter **20**, 434221 (2008).
[18] C.-W. Nan, M. I. Bichurin, S. Dong, D. Viehland, and G. Srinivasan, J. Appl. Phys. **103**, 031101 (2008).
[19] G. Catalan and J. F. Scott, Adv. Mater. **21**, 2463 (2009).
[20] J. Ma, J. Hu, Z. Li, and C. W. Nan, Adv. Mater. **23**, 1062 (2011).
[21] T. Kimura, T. Goto, H. Shintani, K. Ishizaka, T. Arima, and Y. Tokura, Nature (London) **426**, 55 (2003).
[22] M. Kenzelmann, A. B. Harris, S. Jonas, C. Broholm, J. Schefer, S. B. Kim, C. L. Zhang, S. W. Cheong, O. P. Vajk, and J. W. Lynn, Phys. Rev. Lett. **95**, 087206 (2005).
[23] H. Katsura, N. Nagaosa, and A. V. Balatsky, Phys. Rev. Lett. **95**, 057205 (2005).
[24] C. Jia, S. Onoda, N. Nagaosa, and J. H. Han, Phys. Rev. B **74**, 224444 (2006).
[25] I. A. Sergienko and E. Dagotto, Phys. Rev. B **73**, 094434 (2006).
[26] I. A. Sergienko, C. Sen, and E. Dagotto, Phys. Rev. Lett. **97**, 227204 (2006).
[27] Y. J. Choi, H. T. Yi, S. Lee, Q. Huang, V. Kiryukhin, and S. W. Cheong, Phys. Rev. Lett. **100**, 047601 (2008).
[28] T.-h. Arima, J. Phys. Soc. Jpn. **76**, 073702 (2007).
[29] H. Murakawa, Y. Onose, S. Miyahara, N. Furukawa, and Y. Tokura, Phys. Rev. Lett. **105**, 137202 (2010).
[30] X. Wang, Y. Chai, L. Zhou, H. Cao, C. D. Cruz, J. Yang, J. Dai, Y. Yin, Z. Yuan, S. Zhang *et al.*, Phys. Rev. Lett. **115**, 087601 (2015).
[31] Y. Long, Chin. Phys. B **25**, 078108 (2016).
[32] Y. Long and Y. Shimakawa, New J. Phys. **12**, 063029 (2010).
[33] M. V. Talanov, Acta Cryst. A **75**, 379 (2019).
[34] G. King and P. M. Woodward, J. Mater. Chem. **20**, 5785 (2010).
[35] J. S. Feng and H. J. Xiang, Phys. Rev. B **93**, 174416 (2016).
[36] J. Wang, J. B. Neaton, H. Zheng, V. Nagarajan, S. B. Ogale, B. Liu, D. Viehland, V. Vaithyanathan, D. G. Schlom, U. V. Waghmare *et al.*, Science **299**, 1719 (2003).
[37] J. B. Neaton, C. Ederer, U. V. Waghmare, N. A. Spaldin, and K. M. Rabe, Phys. Rev. B **71**, 014113 (2005).
[38] R. Seshadri and N. A. Hill, Chem. Mater. **13**, 2892 (2001).
[39] A. M. dos Santos, S. Parashar, A. R. Raju, Y. S. Zhao, A. K. Cheetham, and C. N. R. Rao, Solid State Commun. **122**, 49 (2002).
[40] T. Kimura, S. Kawamoto, I. Yamada, M. Azuma, M. Takano, and Y. Tokura, Phys. Rev. B **67**, 180401(R) (2003).
[41] L. Zhou, J. Dai, Y. Chai, H. Zhang, S. Dong, H. Cao, S. Calder, Y. Yin, X. Wang, X. Shen *et al.*, Adv. Mater. **29**, 1703435 (2017).
[42] A. C. Larson and R. B. Von Dreele, General structure analysis system (GSAS), Report No. LAUR 86–748, Los Alamos National Laboratory, Los Alamos, NM, 1994.
[43] Y. Long, T. Saito, M. Mizumaki, A. Agui, and Y. Shimakawa, J. Am. Chem. Soc. **131**, 16244 (2009).
[44] C. Mitra, Z. Hu, P. Raychaudhuri, S. Wirth, S. I. Csiszar, H. H. Hsieh, H. J. Lin, C. T. Chen, and L. H. Tjeng, Phys. Rev. B **67**, 092404 (2003).
[45] A. N. Vasiliev, O. S. Volkova, L. S. Lobanovskii, I. O. Troyanchuk, Z. Hu, L. H. Tjeng, D. I. Khomskii, H. J. Lin, C. T. Chen, N. Tristan *et al.*, Phys. Rev. B **77**, 104442 (2008).
[46] E. Pellegrin, L. H. Tjeng, F. M. F. de Groot, R. Hesper, G. A. Sawatzky, Y. Moritomo, and Y. Tokura, J. Electron Spectrosc. Relat. Phenom. **86**, 115 (1997).
[47] N. Hollmann, Z. Hu, T. Willers, L. Bohatý, P. Becker, A. Tanaka, H. H. Hsieh, H.-J. Lin, C. T. Chen, and L. H. Tjeng, Phys. Rev. B **82**, 184429 (2010).
[48] S. Nemrava, D. A. Vinnik, Z. Hu, M. Valldor, C. Y. Kuo, D. A. Zherebtsov, S. A. Gudkova, C. T. Chen, L. H. Tjeng, and R. Niewa, Inorg. Chem. **56**, 3861 (2017).
[49] Y. U. Idzerda, L. H. Tjeng, H.-J. Lin, C. J. Gutierrez, G. Meigs, and C. T. Chen, Phys. Rev. B **48**, 4144 (1993).
[50] J. Chen, X. Wang, Z. Hu, L. H. Tjeng, S. Agrestini, M. Valvidares, K. Chen, L. Nataf, F. Baudelet, M. Nagao *et al.*, Phys. Rev. B **102**, 184418 (2020).
[51] T. Burnus, Z. Hu, H. H. Hsieh, V. L. J. Joly, P. A. Joy, M. W. Haverkort, H. Wu, A. Tanaka, H.-J. Lin, C. T. Chen, and L. H. Tjeng, Phys. Rev. B **77**, 125124 (2008).
[52] J. P. Rivera, Eur. Phys. J. B **71**, 299 (2009).
[53] H. Grimmer, Ferroelectrics **161**, 181 (1994).

[54] Y. F. Popov, A. M. Kadomtseva, S. S. Krotov, D. V. Belov, G. P. Vorob'ev, P. N. Makhov, and A. K. Zvezdin, Low Temp. Phys. **27**, 478 (2001).

[55] T. Kurumaji, S. Ishiwata, and Y. Tokura, Phys. Rev. B **95**, 045142 (2017).

[56] Y. S. Tang, S. M. Wang, L. Lin, C. Li, S. H. Zheng, C. F. Li, J. H. Zhang, Z. B. Yan, X. P. Jiang, and J. M. Liu, Phys. Rev. B **100**, 134112 (2019).

[57] S. Shtrikman and D. Treves, Phys. Rev. **130**, 986 (1963).